

Mechanism of $\text{CeMgAl}_{11}\text{O}_{19}:\text{Tb}^{3+}$ alkaline fusion with sodium hydroxide

Hu Liu, Shen-Gen Zhang*, De-An Pan,
Yi-Fan Liu, Bo Liu, Jian-Jun Tian,
Alex A. Volinsky

Received: 25 September 2014/Revised: 14 November 2014/Accepted: 19 December 2014/Published online: 5 February 2015
© The Nonferrous Metals Society of China and Springer-Verlag Berlin Heidelberg 2015

Abstract Comprehensive $\text{CeMgAl}_{11}\text{O}_{19}:\text{Tb}^{3+}$ (CTMA) disintegration via alkaline fusion was discussed. The rare earth (RE) elements in CTMA were dissolved by HCl completely after alkaline fusion. Relationships between the alkaline fusion temperature and various properties of the compounds were examined by various techniques to elucidate their roles in the expected CTMA disintegration. X-ray diffraction (XRD) analysis indicates the phase transformation sequence. A scientific hypothesis of crystal structure disintegration presents that sodium ions substitute for the europium and barium ions in the mirror plane and magnesium ions in the spinel block successively, resulting in that more oxygen vacancies and interstitial sodium ions appear. The unit cell [$P63/mmc$ (194)] breaks from the mirror plane. Then it is decomposed into NaAlO_2 , and magnesium, cerium, and terbium ions combine with free OH^- into MgO , Tb_2O_3 and CeO_2 ; Tb_2O_3 and CeO_2 change into $\text{Ce}_{0.6}\text{Tb}_{0.4}\text{O}_{2-x}$. In the end, the rare earth oxide is recycled easily by the acidolysis. The mechanism provides fundamental basis for recycling of REEs from waste phosphors.

Keywords Alkaline fusion mechanism; Recycle; $\text{CeMgAl}_{11}\text{O}_{19}:\text{Tb}^{3+}$; Structure transformations

H. Liu, S.-G. Zhang*, D.-A. Pan, Y.-F. Liu, B. Liu, J.-J. Tian
Institute for Advanced Materials and Technology, School of
Materials Science and Engineering, University of Science and
Technology Beijing, Beijing 100083, China
e-mail: zhangshengen@mater.ustb.edu.cn

A. A. Volinsky
Department of Mechanical Engineering, University of South
Florida, Tampa, FL 33620, USA

1 Introduction

Rare earth (RE) elements were becoming increasingly important in the transition to a green, low-carbon economy [1–4]. Waste phosphor attracts considerable attention as a material for recycling REEs due to a large amount of REEs [5]. REEs, especially terbium, are the most critical raw materials, with the highest supply risk in Refs. [6, 7]. From now on, many researches start on REEs recycling from waste phosphor; however, less than 1 % of the REEs were recycled in 2011 [8]. Technically, Ce and Tb in the $\text{CeMgAl}_{11}\text{O}_{19}:\text{Tb}^{3+}$ (CTMA) are difficult to recycle by leaching or mechanochemical treatment due to their stable aluminate crystal structure [9–13].

As is known to all, CTMA has a distorted magnetoplumbite structure. Figure 1 shows the unit cell of magnetoplumbite [14]. The structure consists of spinel-like blocks separated by mirror planes. The spinel blocks are composed of Al^{3+} and O^{2-} , while the mirror planes contain O^{2-} and large ions that are often trivalent rare earth cations. In the unit cell of CTMA, the rare earth ions such as Tb^{3+} incorporated as activators in the phosphors are built into the mirror planes at the site of the large cations such as Ce^{3+} . The Mg^{2+} is located at Al^{3+} sites in the spinel-like blocks. The Al^{3+} sites in the aluminates are of three different types which are in octahedral, tetrahedral, and fivefold surrounding of oxygen ions, respectively [15].

The alkaline fusion of waste phosphor as a pretreatment process makes it possible to increase the leaching rate [16, 17]. However, there are few literatures on the CTMA alkaline fusion mechanism from a viewpoint on structure. Therefore, the mechanism of CTMA via fusion with sodium hydroxide was discussed in this study.

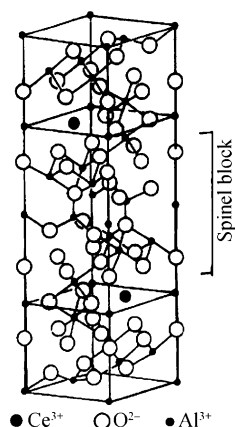
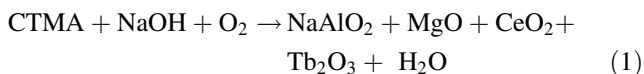


Fig. 1 Projection of unit cells of magnetoplumbite

2 Experimental

In this study, CTMA powders with the average particle size of 2–4 μm were obtained from the Dalian Luminglight, China. CTMA powders were mixed with sodium hydroxide, according to the 1:1 NaOH/CTMA mass ratio by ball milling. Differential scanning calorimetry (DSC) and thermogravimetric (TG) analysis were carried out using the NETZSCH STA 409 C/CD thermal analyzer. The reference material was $\alpha\text{-Al}_2\text{O}_3$ powder, and the parent glass powder samples (<74 μm) were heated from 23 to 700 $^\circ\text{C}$ at the heating rate of 10 $^\circ\text{C}\cdot\text{min}^{-1}$. The mixtures were then placed into 200 ml iron crucibles. Fusion was performed in the furnace at 150, 200, 250, 275, 300, 325 and 350 $^\circ\text{C}$ for 2 h separately, and quenching processing was needed to keep the crystal structure in the condition. The main chemical reaction during the alkali fusion process is:



The fusion product was cleaned several times by stirring at 200 $\text{r}\cdot\text{min}^{-1}$ for 20 min with deionized water at 60 $^\circ\text{C}$ to remove NaOH and NaAlO₂. All of the intermediate and final products obtained were collected and dry roasted at 120 $^\circ\text{C}$, and then ground to particle size of smaller than 52 μm . X-ray diffraction (XRD) analysis was performed using Philips APD-10 X-ray diffractometer with Cu $K\alpha$ radiation, 40 kV voltage, and 150 mA current at 10 min^{-1} scanning rate, with 2θ range of 10 $^\circ$ –100 $^\circ$. The morphology and the mean particle size were observed by scanning electron microscope (SEM, JSM-6510A, Japan).

3 Results and discussion

3.1 Simultaneous thermal analysis

Figure 2 shows the typical DSC–TG curves of the mixture. From the TG curve, the total weight loss between room

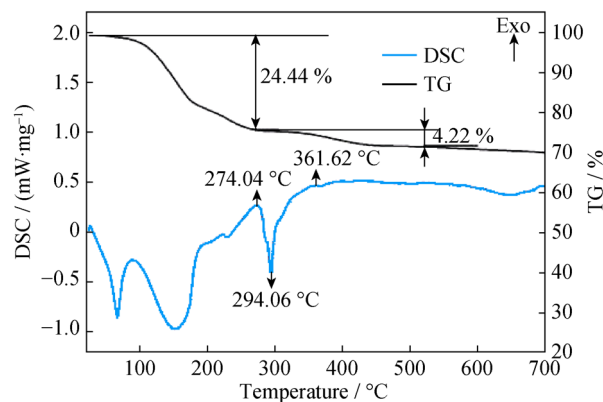


Fig. 2 DSC–TG curves of mixture (CTMA) under flowing air

temperature (RT) and 274.04 $^\circ\text{C}$ is measured to be about 24.44 %, and it is the evaporation of water due to high moisture-absorption of sodium hydroxide. And there is an endothermic peak at 150 $^\circ\text{C}$ and a turning point at 200 $^\circ\text{C}$ in both the TG and DSC curves, at which the reaction may begin. However, the DSC curve shows an exothermic peak located at 274.04 $^\circ\text{C}$ and the maximum endothermic peak located at 294.06 $^\circ\text{C}$, which means that the alkaline fusion process takes place at 274.04 $^\circ\text{C}$ and finishes at 294.06 $^\circ\text{C}$. According to the TG curve, the weight loss between 274.04 and 400.00 $^\circ\text{C}$ is measured to be about 4.22 %, and the DSC curve shows an endothermic peak located at 310.9 $^\circ\text{C}$. The temperature range of the endothermic peak in the DSC curve fits well with that of weight loss in the TG curve, which means that the reaction starts at 150 $^\circ\text{C}$ and finishes at about 400 $^\circ\text{C}$.

3.2 Phase and microstructural analyses

Figure 3 shows XRD patterns of alkaline fusion CTMA products at different temperatures. The product were treated by washing. When the temperature is lower than 250 $^\circ\text{C}$, the main crystal phase hardly changes due to the low reaction rate between solid phases at low temperature. When the alkali temperature increases to 300 $^\circ\text{C}$, diffraction peak intensities of CTMA significantly reduce, and the main crystal phase is CTMA phase, but the $\text{Ce}_{0.6}\text{Tb}_{0.4}\text{O}_{2-x}$ phase appears. It shows that CTMA phase starts to decompose, but not completely. When the alkali temperature increases to 325 $^\circ\text{C}$, even 350 $^\circ\text{C}$, diffraction peak of CTMA disappears, and the main crystal phases are $\text{Ce}_{0.6}\text{Tb}_{0.4}\text{O}_{2-x}$ (JCPDS 52-1303), Tb_2O_3 (JCPDS 23-1418) and MgO (JCPDS 45-0946).

However, from the details of the XRD patterns at different temperatures in Fig. 4, when the temperature increases, the CTMA diffraction peak splits and shifts to large angle in Fig. 4a. The results show the decrease of

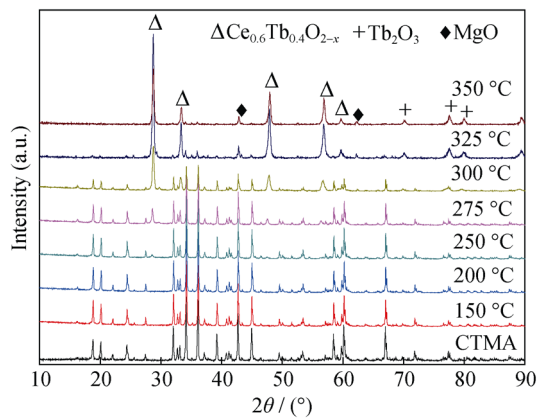


Fig. 3 XRD patterns of alkaline fusion production at different temperatures

CTMA crystalline size and significant phase transformation. And the diffraction peak intensities of CTMA significantly reduce. From Fig. 4b, the diffraction peak of CeO₂ (JCPDS 34-0394) first appears at 275 °C, and those of Tb₂O₃ (JCPDS 23-1418), Ce_{0.6}Tb_{0.4}O_{2-x} and MgO

(JCPDS 45-0946) first appear at 300, 325, and 325 °C, respectively, which fit well with DSC–TG curves in Fig. 2.

The phase analysis from Fig. 4 is listed in Table 1. According to the results of XRD analysis, the transformation of the crystalline structure in the alkaline fusion process is shown in Fig. 5. It shows that, firstly, Tb and Mg in CTMA [*P63/mmc* (194)] move from the crystal lattice, and the main phase changes into CeAl₁₁O₁₈ [JCPDS 48-0055, *P63/mmc* (194)]. And then they are decomposed into NaAlO₂ and CeO₂ with the reaction. Increasing temperature benefits the formation of Ce_{0.6}Tb_{0.4}O_{2-x} from Tb₂O₃ and CeO₂. The details of phases' crystalline structures are obtained from Table 2. It shows that the CTMA is decomposed step by step in the alkaline fusion process.

Figure 6 shows SEM images of CTMA and alkaline fusion product at different temperatures. The raw CTMA are irregular particles with smooth surface and size of 2–4 μm as depicted in Fig. 6a. However, the smooth surface becomes rough after alkaline fusion at 275 °C as shown in Fig. 6b, but the particles are complete. When the alkaline fusion occurs at 300 or 325 °C as shown in Fig. 6c,

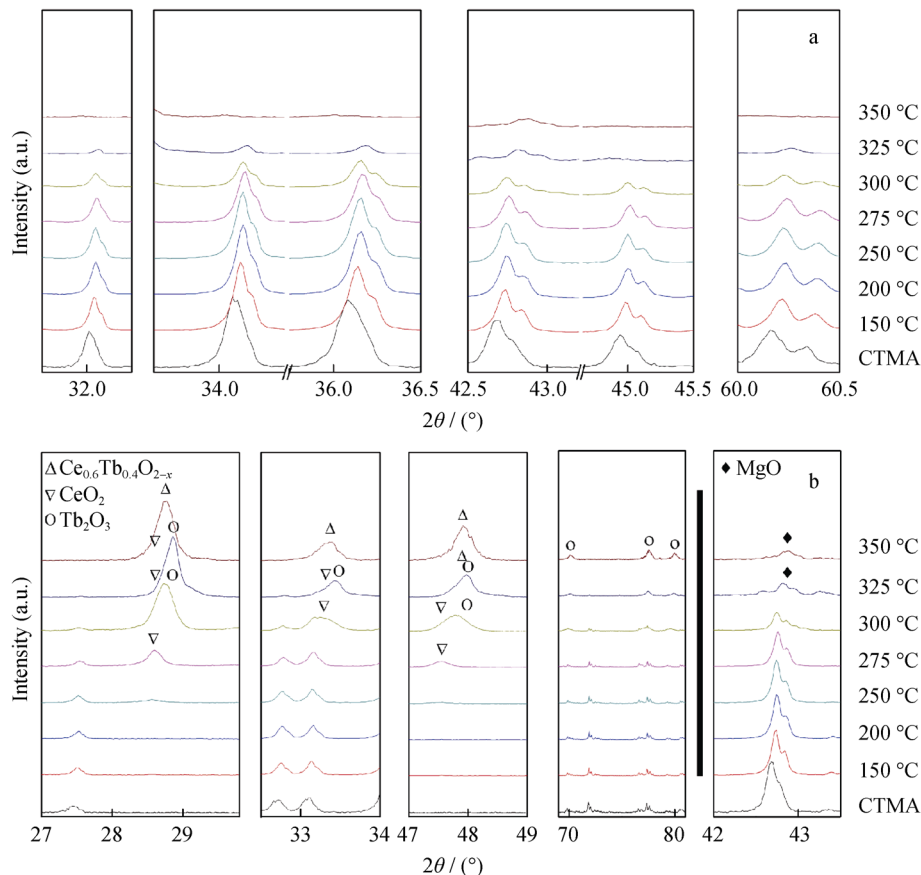


Fig. 4 Details of XRD patterns at different temperatures: **a** CTMA phase transition process and **b** product phases

d, the particles are disintegrated gradually and finally break into smaller grains with the size of 300–400 nm, but are severely agglomerated.

Table 1 Transformation of crystalline structure in alkaline fusion process

$T/^\circ\text{C}$	Phases
RT	$\text{CeMgAl}_{11}\text{O}_{19}$; Tb^{3+}
150–250	$\text{CeMgAl}_{11}\text{O}_{19}$; Tb^{3+} , $\text{CeAl}_{11}\text{O}_{18}$
275	$\text{CeMgAl}_{11}\text{O}_{19}$; Tb^{3+} , $\text{CeAl}_{11}\text{O}_{18}$, CeO_2 , (NaAlO_2)
300	$\text{CeMgAl}_{11}\text{O}_{19}$; Tb^{3+} , $\text{CeAl}_{11}\text{O}_{18}$, CeO_2 , $\text{Ce}_{0.6}\text{Tb}_{0.4}\text{O}_{2-x}$, (NaAlO_2)
325	$\text{CeAl}_{11}\text{O}_{18}$, CeO_2 , $\text{Ce}_{0.6}\text{Tb}_{0.4}\text{O}_{2-x}$, Tb_2O_3 , MgO , (NaAlO_2)
350	CeO_2 , $\text{Ce}_{0.6}\text{Tb}_{0.4}\text{O}_{2-x}$, Tb_2O_3 , MgO , (NaAlO_2)

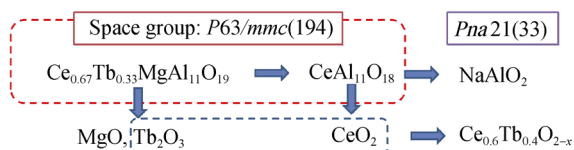


Fig. 5 Phases transition in alkaline fusion process

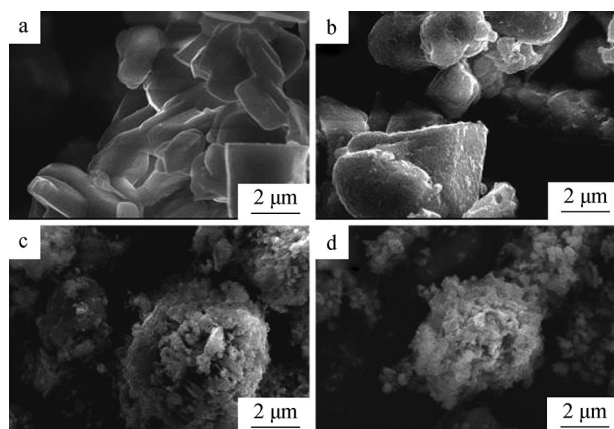


Fig. 6 SEM images of CTMA and alkaline fusion product at different temperatures: **a** CTMA before alkaline fusion, **b** 275 °C, **c** 300 °C, and **d** 325 °C

3.3 Acid soluble analyses

The products were dissolved completely in $2 \text{ mol}\cdot\text{L}^{-1}$ HCl after alkaline fusion at 500 °C for 2 h with the solid-to-liquid ratio of 1:5, temperature of 60 °C, and time of 2 h. The rare earth oxide (REO) would be recycled by oxalic acid precipitation and calcination. It means that the alkaline fusion is an effective method for recycling of Ce and Tb from CTMA.

3.4 Model and mechanism analyses

From the SEM results obtained at the “macro” level, it is reasonable to conclude that the alkaline fusion process can be described by the shrinking core model [18]. Figure 7 illustrates the model of the mechanism of the alkaline fusion reaction. It is hypothesized that: (1) NaOH turns into molten salt at about 300 °C; (2) the reaction occurs on the surface of the particle, and the product diffuses into the surrounding liquid phase; (3) then the surface becomes rougher with small pores and cracks, particularly for the particle with a high conversion rate; (4) the reaction proceeds until the decomposition of particle is completed, in the end, the smaller grains aggregate in the liquid phase.

At the “micro” level, Fig. 8 illustrates the basic premises of the mechanism of unit cell. When the NaOH melts to ion liquid, Na^+ may substitute for RE ion sites in mirror plane initially, due to that Na^+ radius of 102 pm is close to that of RE ions (Ce^{3+} 103.4 pm, Tb^{3+} 92.3 pm). Then the RE ions combine with free OH^- into REO and H_2O .

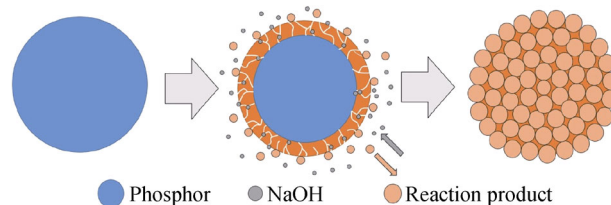


Fig. 7 Schematic representation of probable mechanism

Table 2 Lattice parameters of phases in alkaline fusion process

Phases	PDF card Nos.	Space groups	a/nm	b/nm	c/nm	$\alpha/^\circ$	$\beta/^\circ$	$\gamma/^\circ$
$\text{CeMgAl}_{11}\text{O}_{19}$; Tb^{3+}	36-0073	$P63/mmc$ (194)	0.5558	0.5558	2.1905	90	90	120
$\text{CeAl}_{11}\text{O}_{18}$	48-0055		0.5558	0.5558	2.2012	90	90	120
NaAlO_2	33-1200	$Pna21$ (33)	0.5387	0.7033	0.5218	90	90	90
CeO_2	34-0394	$Fm-3m$ (225)	0.5411	0.5411	0.5411	90	90	90
Tb_2O_3	23-1418	$La-3$ (206)	1.0730	1.0730	1.0730	90	90	90
$\text{Ce}_{0.6}\text{Tb}_{0.4}\text{O}_{2-x}$	52-1303	F	0.5394	0.5394	0.5394	90	90	90
MgO	45-0946	$Fm-3m$ (225)	0.4211	0.4211	0.4211	90	90	90

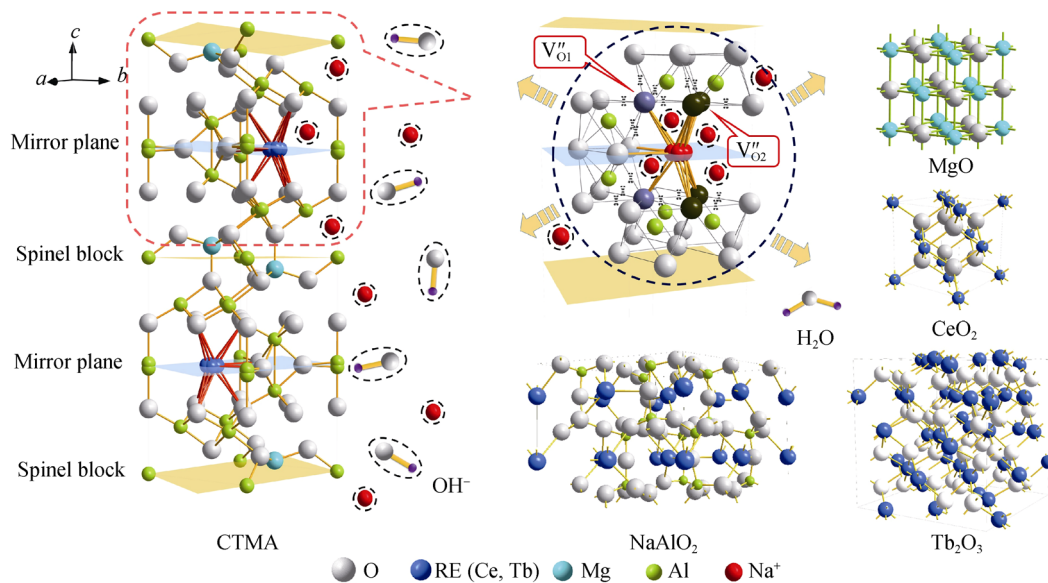


Fig. 8 Probable mechanism of CTMA unit cell

However, it results in much more defects around the sodium ion sites due to their different valence states, such as interstitial sodium ions and oxygen vacancies. The lattice constant of the mirror plane increases, and oxygen vacancies, sharing in the sites of vertex (V''_{O1}) and edges (V''_{O2}) in alumina octahedral, would be produced, which will break the structure of spinel block. The defect generally provides an extensive perturbation of the surrounding lattice; it would increase the diffusion amount of Na^+ . The neighboring oxygen ions, the aluminum ions, and Na^+ regroup to NaAlO_2 in the spinel blocks, and Mg^{2+} would combine with free OH^- into MgO and H_2O .

4 Conclusion

The mechanism of $\text{CeMgAl}_{11}\text{O}_{19}$: Tb^{3+} alkaline fusion with sodium hydroxide was examined by various techniques to elucidate their roles in the expected BMA transformations. XRD analysis indicates that the transformation sequence involves $\text{CeAl}_{11}\text{O}_{18}$ as the intermediate phases between CTMA and the final product. Because sodium ions substitute for the cerium and terbium ions in the mirror plane during the process, more oxygen vacancies and interstitial sodium ions produce and cause the unit cell [$P63/mmc$ (194)] to break from the mirror plane. Then during the process sodium ions substitute for the magnesium ions in the spinel block successively. Finally, the CTMA is decomposed into NaAlO_2 , CeO_2 , Tb_2O_3 , and MgO . At the same time, some of CeO_2 and Tb_2O_3 continue to form $\text{Ce}_{0.6}\text{Tb}_{0.4}\text{O}_{2-x}$.

Acknowledgments The work was financially supported by the National Key Project of the Scientific and Technical Support Program of China (No. 2012BAC02B01), the National Hi-Tech R&D Program of China (No. 2012AA063202), the National Natural Science Foundation of China (No. 51472030), the Fundamental Research Funds for the Central Universities (Project No. FRF-TP-14-043A1), and the China Postdoctoral Science Foundation Funded Project (No. 2014M560885).

References

- [1] Humphries M. Rare Earth Elements: the Global Supply Chain. Washington, D.C: DIANE Publishing; 2010. 2.
- [2] Xu KD, Ren ZM, Li CJ. Progress in application of rare metals in superalloys. *Rare Met.* 2014;33(2):111.
- [3] Yang C, Hou YL. Advance in the chemical synthesis and magnetic properties of nanostructured rare-earth-based permanent magnets. *Rare Met.* 2013;32(2):105.
- [4] Reddy YS, Kiataiah P. Elastic properties of double layered manganites $\text{R}_{1.2}\text{Sr}_{1.8}\text{Mn}_2\text{O}_7$ (R = La, Pr, Nd, Sm). *Rare Met.* 2014;33(2):166.
- [5] Bünzli JCG, Pecharsky VK. Handbook on the Physics and Chemistry of Rare Earths, vol. 43. North Holland: Elsevier; 2013. 182.
- [6] European Commission. Critical raw materials for the EU. report of the ad-hoc working group on defining critical raw materials. (EC, Ed.). Brussels, 2010, 23.
- [7] Bauer D, Diamond D, Li J. Critical Materials Strategy. Washington, D.C: Department of Energy; 2011. 97.
- [8] Binnemans K, Jones PT, Blanpain B, Van GT, Yang Y, Walton A, Buchert M. Recycling of rare earths: a critical review. *J. Clean Prod.* 2013;51:1.
- [9] Zhang Q, Saito F. Non-thermal extraction of rare earth elements from fluorescent powder by means of its mechanochemical treatment. *J Min Mater Inst Jpn.* 1998;114:253.
- [10] Zhang Q, Lu J, Saito F. Selection extraction of Y and Eu by non-thermal acid leaching of fluorescent powder activated by mechanochemical treatment using a planetary mill. *J Min Mater Inst Jpn.* 2000;1162:137.

- [11] Takahashi T, Takano A, Saitoh T, Shigen-to-Sozai. Separation and recovery of rare earth elements from phosphor sludge in processing plant of waste fluorescent lamp by pneumatic classification and sulfuric acidic leaching. *J Min Mater Inst Jpn.* 2001;117:579.
- [12] Shimizu R, Sawada K, Enokida Y, Yamamoto I. Supercritical fluid extraction of rare earth elements from luminescent material in waste fluorescent lamps. *J Supercrit Fluids.* 2005;33(3):235.
- [13] Horikawa T, Machida K. Reuse and recycle processing for rare earth phosphors. *Mater Integr.* 2011;24:37.
- [14] Stevels ALN. Ce^{3+} luminescence in hexagonal aluminates containing large divalent or trivalent cations. *J Electrochem Soc.* 1978;125(4):588.
- [15] Zhang J, Zhang Z, Tang Z, Lin Y. Mn^{2+} luminescence in (Ce, Tb) $MgAl_{11}O_{19}$ phosphor. *Mater Chem Phys.* 2001;72(1):81.
- [16] Liu H, Zhang S, Tian J, Yang M, Wu ML, Volinsky AA. Rare earth elements recycling from waste phosphor by dual hydrochloric acid dissolution. *J Hazard Mater.* 2014;272:96.
- [17] Zhang SG, Yang M, Liu H, Pan D, Tian JJ. Recovery of waste rare earth fluorescent powders by two steps acid leaching. *Rare Met.* 2013;32(6):609.
- [18] Mgaidi A, Jendoubi F, Oulahna D, Maaoui MEI, Dodds JA. Kinetics of the dissolution of sand into alkaline solutions: application of a modified shrinking core model. *Hydrometallurgy.* 2004;71(3):435.